

# Discrete Orthogonal Decomposition and Variational Fluid Flow Estimation

Jing Yuan · Christoph Schnörr · Etienne Mémin

Published online: 20 June 2007  
© Springer Science+Business Media, LLC 2007

**Abstract** We exploit the mimetic finite difference method introduced by Hyman and Shashkov to present a framework for estimating vector fields and related scalar fields (divergence, curl) of physical interest from image sequences. Our approach provides a basis for consistent definitions of higher-order differential operators, for the analysis and a novel stability result concerning second-order div-curl regularizers, for novel variational schemes to the estimation of solenoidal (divergence-free) image flows, and to convergent numerical methods in terms of subspace corrections.

**Keywords** Variational models · Optical flow · Helmholtz decomposition · Experimental fluid dynamics

## 1 Introduction

The estimation of highly non-rigid image flows is an important problem in various application areas of image analysis like remote sensing, medical imaging, and experimental fluid mechanics. Such flows, which cannot be represented by a single parametric model, are typically estimated by variational approaches. In contrast to standard approaches, however, higher-order regularization is necessary in order to accurately recover important flow structures like vortices, for

example, and to incorporate physically plausible constraints, like vanishing divergence of the flow.

The basis for our paper is early work on second-order regularizers constraining the gradients of the flow components divergence and curl [1, 11, 20]. This regularization approach has been elaborated in a series of papers by Mémin and co-workers [8, 9]. Moreover, the decomposition and representation of *continuous* vector fields by velocity potentials and stream functions [10] has been adopted to derive piecewise parametric representations of relevant flow structures. Recently, the direct estimation of this representation from image sequences has been studied in [16].

The objective of this contribution is to provide a mathematically sound discrete representation of vector fields in terms of basic flow components related to quantities of physical relevance, and a corresponding decomposition into subspaces of the linear space of discrete vector valued functions. By this, we obtain and can investigate a discrete analogue of known continuous representations [10] in connection with image sequence analysis of fluids. This gives rise, for example, to a novel variational approach for estimation solenoidal (divergence-free) flows from image sequences. Furthermore, we remove numerical convergence problems of the heuristic alternating numerical estimation scheme employed in [16] by adopting a subspace correction method from numerical analysis which directly applies to our flow field representation. Finally, our analysis reveals the importance of an additional boundary regularization term in connection div-curl regularizers (Sect. 4.3), which has been overlooked apparently in previous work.

In Sect. 2, we present the discrete representation of both scalar and vector fields based on the mimetic finite difference method introduced by Hyman and Shashkov [12, 13]. A basic feature of this representation is that basic integral

J. Yuan (✉) · C. Schnörr  
CVGPR Group, University of Mannheim, Mannheim, Germany  
e-mail: yuanjing@uni-mannheim.de

C. Schnörr  
e-mail: schnoerr@uni-mannheim.de

E. Mémin  
VISTA Group, INRIA/IRISA Rennes, Rennes, France  
e-mail: Etienne.Memin@irisa.fr

identities of vector analysis are preserved after discretization. Furthermore, basic first-order differential operators can be defined such that compound higher-order operators with compatible domains and image spaces can be consistently defined. Subsequently, we elaborate the representation of vector fields by potential and stream functions and various useful subspace decompositions of the linear space of discrete vector fields.

Based on this, we reconsider a few variational approaches to motion estimation in Sect. 3. By defining all quantities in terms of the representation developed in Sect. 2, we examine well-posedness and stability, including the non-trivial stability issue mentioned above (Sect. 4). Section 5 provides a natural numerical estimation approach which directly fits to the flow field representation, along with details of the multilevel implementation. We validate our approach with numerical experiments in Sect. 6.

A preliminary conference version of this paper appeared in [28].

## 2 Vector-Field Representation

### 2.1 Discrete Fields and Differential Operators

We use the *mimetic finite difference method* introduced by Hyman and Shashkov [12, 13] in order to preserve basic relationships of continuous vector analysis by appropriately defining their discrete analogues. This scheme applies to general curvilinear grids in two and three dimensions. Here, we only apply it to the special case of rectangular grids. This discretization scheme will be used in Sect. 2.2 to accurately represent and decompose vector fields.

*Linear Spaces.* Figure 1 illustrates the definitions of the following finite-dimensional vector spaces of scalar and vector fields that naturally appear in discrete models of continuum mechanics:

- $H_V$ : the space of *scalar fields* defined on cells,
- $H_P$ : the space of *scalar fields* defined on vertices,
- $H_E$ : the space of *vector fields* defined tangential to sides,
- $H_S$ : the space of *vector fields* defined normal to sides.

We denote with  $H_P^o$ ,  $H_S^o$ ,  $H_E^o$  the subspaces of inner scalar and inner vector fields, respectively, obtained by restricting the spaces  $H_P$ ,  $H_S$ ,  $H_E$ , and by imposing zero boundary values.

*Notation.* We denote with  $L_{i,j+1/2}$  the side between vertices  $(i, j)$  and  $(i, j + 1)$ . The relationship between vertex indices and cell indices is depicted in Fig. 1 for the lower-right cell, denoted with  $\Omega_{i+1/2,j+1/2}$ . To simplify notation, we index cell (side, vertex) positions sometimes directly with  $(\alpha, \beta)$  if the meaning is unambiguous.  $\Omega$  denotes the whole image section, and  $\partial\Omega$  its boundary,

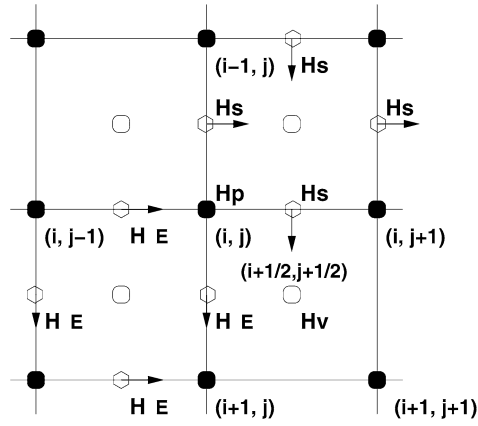


**Fig. 1** Definition of finite-dimensional spaces of scalar fields and vector fields on a rectangular grid. Filled circles depict *nodes* or *vertices*, the other circles indicate *cells*. The positions of diamonds are referred to as *sides*

*Convention.* We consider in this paper only regular grids with unit side-lengths  $L_{\alpha,\beta} = 1$  and unit cell-areas  $\Omega_{\alpha,\beta} = 1$ ,  $\forall \alpha, \beta$ . Let our grid consist of  $m \times n$  vertices. Reshaping the scalar/vector fields columnwise into vectors, we identify:  $H_P = \mathbb{R}^{mn}$ ,  $H_P^o = \mathbb{R}^{(m-2)(n-2)}$ ,  $H_V = \mathbb{R}^{(m-1)(n-1)}$ ,  $H_S = \mathbb{R}^{m(n-1)+n(m-1)}$ ,  $H_S^o = \mathbb{R}^{(m-1)(n-2)+(n-1)(m-2)}$ , and  $H_E$ ,  $H_E^o$  with  $H_S$ ,  $H_S^o$ .

*Inner products and Norms.* While  $H_P$  and  $H_V$  are equipped with the usual Euclidian inner product

$$\langle g, h \rangle_{H_V} = \sum_{\Omega_{\alpha,\beta} \in \Omega} g_{\alpha,\beta} h_{\alpha,\beta},$$

and with the corresponding induced norm, the inner products on  $H_S$  and  $H_E$  are defined as follows: let the indices  $D, T, R, L$  refer to the sides of cell  $\Omega_{\alpha,\beta}$ ,  $u \in H_S$ , and

$$u_{\Omega_{\alpha,\beta}} := \frac{1}{\sqrt{2}}(u_D, u_T, u_R, u_L)_{\alpha,\beta}^T.$$

Then

$$\langle u, v \rangle_{H_S} := \sum_{\Omega_{\alpha,\beta} \in \Omega} \langle u_{\Omega_{\alpha,\beta}}, v_{\Omega_{\alpha,\beta}} \rangle, \quad \|u\|_{H_S} := \sqrt{\langle u, u \rangle_{H_S}}.$$

Analogous definitions hold for  $H_E$ .

*First-order Differential Operators.* We define the discrete first-order differential operators corresponding to  $\nabla$ ,  $\nabla^\perp$ ,  $\text{div}$ , and  $\text{curl}$ , operating on discretized 2D data:

$$\mathbb{G} : H_P \rightarrow H_E, \quad \mathbb{G}^\perp : H_P \rightarrow H_S, \quad (1a)$$

$$\text{Div} : H_S \rightarrow H_V, \quad \text{Curl} : H_E \rightarrow H_V,$$

$$\overline{\mathbb{G}} : H_{V+\partial V} \rightarrow H_S, \quad \overline{\mathbb{G}}^\perp : H_{V+\partial V} \rightarrow H_E, \quad (1b)$$

$$\overline{\text{Div}} : H_E^o \rightarrow H_P^o, \quad \overline{\text{Curl}} : H_S^o \rightarrow H_P^o.$$

Let

$$\mathbf{D}_m := \begin{pmatrix} -1 & 1 & 0 & \dots & 0 & 0 & 0 \\ 0 & -1 & 1 & \dots & 0 & 0 & 0 \\ & \ddots & \ddots & \ddots & & & \\ 0 & 0 & 0 & \dots & -1 & 1 & 0 \\ 0 & 0 & 0 & \dots & 0 & -1 & 1 \end{pmatrix} \in \mathbb{R}^{m-1,m},$$

and

$$\tilde{\mathbf{D}}_m := \begin{pmatrix} -2 & 2 & 0 & 0 & \dots & 0 & 0 & 0 & 0 \\ 0 & -1 & 1 & 0 & \dots & 0 & 0 & 0 & 0 \\ 0 & 0 & -1 & 1 & \dots & 0 & 0 & 0 & 0 \\ & \ddots & \ddots & \ddots & & & & & \\ 0 & 0 & 0 & 0 & \dots & -1 & 1 & 0 & 0 \\ 0 & 0 & 0 & 0 & \dots & 0 & -1 & 1 & 0 \\ 0 & 0 & 0 & 0 & \dots & 0 & 0 & -2 & 2 \end{pmatrix} \in \mathbb{R}^{m,m+1}.$$

Then the discrete operators are represented by the following matrices

$$\mathbb{G} = \begin{pmatrix} \mathbf{I}_n \otimes \mathbf{D}_m \\ \mathbf{D}_n \otimes \mathbf{I}_m \end{pmatrix}, \quad \overline{\mathbb{G}} = \begin{pmatrix} \mathbf{I}_{n-1} \otimes \tilde{\mathbf{D}}_m \\ \tilde{\mathbf{D}}_n \otimes \mathbf{I}_{m-1} \end{pmatrix},$$

$$\mathbb{Div} = (\mathbf{I}_{n-1} \otimes \mathbf{D}_m, \mathbf{D}_n \otimes \mathbf{I}_{m-1}),$$

$$\overline{\mathbb{Div}} = (\mathbf{I}_{n-2} \otimes \mathbf{D}_{m-1}, \mathbf{D}_{n-1} \otimes \mathbf{I}_{m-2}),$$

$$\mathbb{Curl} = (\mathbf{D}_n \otimes \mathbf{I}_{m-1}, -\mathbf{I}_{n-1} \otimes \mathbf{D}_m),$$

$$\overline{\mathbb{Curl}} = (\mathbf{D}_{n-1} \otimes \mathbf{I}_{m-2}, -\mathbf{I}_{n-2} \otimes \mathbf{D}_{m-1}),$$

where  $\otimes$  denotes the Kronecker product of matrices. The operator  $\mathbb{G}^\perp : H_P \rightarrow H_S$  is defined by

$$\mathbb{G}^\perp = \begin{pmatrix} -\mathbf{D}_n \otimes \mathbf{I}_m \\ \mathbf{I}_n \otimes \mathbf{D}_m \end{pmatrix}.$$

It is easy to check that the restricted operator  $\mathbb{G}^\perp|_{H_S^0}$  maps to  $H_S^0$ .

Finally, for discretizing the boundary condition,  $\mathbf{n} \cdot \mathbf{u}|_{\partial\Omega}$ , we introduce the boundary operator

$$\mathbb{B}_n : H_S \rightarrow \partial H_S := H_S \setminus H_S^0,$$

which restricts the vector field to the vectors at the grid's boundary multiplied by the outer normal vectors. The matrix form of the boundary operator is:

$$\mathbb{B}_n = \begin{pmatrix} \mathbf{I}_{n-1} \otimes \mathbf{B}_m & \mathbf{0} \\ \mathbf{0} & \mathbf{B}_n \otimes \mathbf{I}_{m-1} \end{pmatrix},$$

where  $\mathbf{0}$  are zero matrices of appropriate sizes, and

$$\mathbf{B}_m := \begin{pmatrix} -1 & 0 & \dots & 0 & 0 \\ 0 & 0 & \dots & 0 & 1 \end{pmatrix} \in \mathbb{R}^{2,m}.$$

It has been shown [13] that using the operators defined above, elementary properties of continuous fields in terms of  $\text{div}$ ,  $\text{curl}$ ,  $\nabla$ , carry over to the discrete case. For example, if the curl of a vector field  $w$  is zero,  $\text{Curl } w \equiv 0$ , then the vector field can be expressed as the gradient of a scalar field  $U$ ,  $w = \mathbb{G}U$ ; or, if the divergence of a vector field  $w$  is a zero,  $\mathbb{Div } w \equiv 0$ , then it should be the curl of another vector field,  $w = \mathbb{G}^\perp U$  (recall that we only consider the 2D case in this paper).

Similarly, Green's theorem

$$\int_{\Omega} g \cdot \text{div } u \, dv + \int_{\Omega} \nabla g \cdot u \, dv = \int_{\partial\Omega} g u_n \, ds \quad (2)$$

becomes in the discrete case

$$\langle g, \mathbb{Div } u \rangle_{H_V} + \langle \overline{\mathbb{G}}g, u \rangle_{H_S} = \sum_{L_{\alpha,\beta} \in \partial\Omega} g_{\alpha,\beta} u_{n;\alpha,\beta}, \quad (3)$$

whereas Gauss' theorem

$$\int_{\Omega} \text{div } u \, dv = \int_{\partial\Omega} u_n \, ds \quad (4)$$

reads in the discrete case

$$\sum_{\Omega_{\alpha,\beta} \in \Omega} \mathbb{Div } u = \sum_{L_{\alpha,\beta} \in \partial\Omega} u_{n;\alpha,\beta}. \quad (5)$$

Using the definitions above, we rewrite this equation more concisely as

$$\mathbf{1}_{\dim H_V}^T \mathbb{Div } u = \mathbf{1}_{\dim \partial\Omega}^T \mathbb{B}_n u, \quad (6)$$

where  $\mathbf{1}_n$  denotes the one-vector.

Most importantly, the additional dual operators (1b) resolve the incompatibilities of domains and ranges of the primal operators (1a) when used to build *compound second order* differential operators (cf. (16) below). For example,  $\mathbb{G}$  and  $\mathbb{Div}$  cannot be regarded as mutually adjoint operators, whereas  $\mathbb{G}$ ,  $\overline{\mathbb{Div}}$  and  $\overline{\mathbb{G}}$ ,  $\mathbb{Div}$  do.

## 2.2 Orthogonal Decomposition

We represent vector fields directly in terms of their irrotational and solenoidal components. These two components are defined by the first-order variations of velocity potentials  $\psi \in H_{V+\partial V}$  and stream functions  $\phi \in H_P$ , and are orthogonal to each other.

**Theorem 2.1** (Basic Vector Field Decomposition [14]) *For any 2D vector field  $u \in H_S$ , the representation of  $u$  in terms of  $\psi, \phi$*

$$u = \overline{\mathbb{G}}\psi + \mathbb{G}^\perp\phi, \quad \mathbb{B}_n u = \mathbb{B}_n \overline{\mathbb{G}}\psi, \quad (7)$$

*where  $\phi_{\partial\Omega} = 0$ , is unique up to a constant of  $\psi$ .*

According to (7), let:

$$u = v + w, \quad v = \overline{\mathbb{G}}\psi, \quad w = \mathbb{G}^\perp\phi.$$

Since the operators defined in the previous section satisfy [12, 13]:

$$\mathbb{D}\text{iv } \mathbb{G}^\perp \equiv 0, \quad \overline{\mathbb{C}\text{url }} \overline{\mathbb{G}} \equiv 0,$$

we have

$$\mathbb{D}\text{iv } w = 0, \quad \overline{\mathbb{C}\text{url }} v = 0, \quad (8)$$

and

$$\langle w, v \rangle_{H_S} = \langle \overline{\mathbb{G}}\psi, \mathbb{G}^\perp\phi \rangle_{H_S} = \langle \overline{\mathbb{C}\text{url }} \overline{\mathbb{G}}\psi, \phi \rangle_{H_P} \equiv 0. \quad (9)$$

This shows:

**Theorem 2.2** (Orthogonality) *The decomposition (7) is orthogonal:*

$$\langle \overline{\mathbb{G}}\psi, \mathbb{G}^\perp\phi \rangle_{H_S} = 0, \quad \forall u \in H_S \quad (10)$$

Defining the corresponding subspaces

$$S_{\text{ir}} := \{u \in H_S | u = \overline{\mathbb{G}}\psi\}, \quad (11)$$

$$S_{\text{sol}} := \{u \in H_S | u = \mathbb{G}^\perp\phi, \phi_{\partial\Omega} = 0\}, \quad (12)$$

the theorem asserts that the direct sum holds:

$$H_S = S_{\text{ir}} \oplus S_{\text{sol}} \quad (13)$$

Representation (7) is motivated by analogous decompositions of continuous vector fields [10]. However, discretizing such vector fields with standard finite differences or finite elements yields *approximate* decompositions only, which may lead to numerical instabilities in applications. In contrast, Theorem 2.1 provides an *exact* orthogonal decomposition of the *finite*-dimensional space of vector fields  $H_S$ . Furthermore, as detailed below, the decomposition allows to estimate  $\psi$  and  $\phi$  directly from a image sequence. Using variational optical flow approaches, the estimation can be done in parallel by applying subspace correction methods. Alternatively, we may first estimate the motion field  $u$ , and then compute  $\psi$  and  $\phi$  in a subsequent step by solving the Neumann and Dirichlet problems

$$\Delta_D \psi = \mathbb{D}\text{iv } u, \quad \mathbb{B}_n \overline{\mathbb{G}}\psi = \mathbb{B}_n u, \quad (14)$$

$$\Delta_C \phi = \overline{\mathbb{C}\text{url }} u, \quad \phi_{\partial\Omega} = 0, \quad (15)$$

where the discrete Laplacians are defined by

$$\Delta_D := \mathbb{D}\text{iv } \overline{\mathbb{G}}, \quad \Delta_C := \overline{\mathbb{C}\text{url }} \mathbb{G}^\perp, \quad (16)$$

and the additional constraint  $\mathbf{1}_{\dim H_V}^T \psi = 0$  (continuous case:  $\int_{\Omega} \psi dv = 0$ ) is used to eliminate the arbitrary constant in (7) and (14).

In the remainder of this paper, however, we show that directly estimating  $\psi, \phi$  from image sequence data is feasible. Throughout we adopt the strategy to express estimation problems by direct relations between the data and unknowns. Such direct formulations allow to formulate hypotheses about unknowns in a proper way and avoid additional approximation errors through the successive application of independent techniques.

### 2.3 Flow Representation

Consider Gauss' theorem (5) and (6) for any vector field  $u \in H_S$ . We say that  $\rho \in H_V$  and  $v \in \partial H_S$  fulfill the *compatibility condition* if

$$\mathbf{1}_{\dim H_V}^T \rho = \mathbf{1}_{\dim \partial H_S}^T v \quad (17)$$

In what follows, we will make use of another flow representation, besides  $u \in H_S$ . To this end, consider the operator  $A : H_S \rightarrow H_V \oplus H_P^o \oplus \partial H_S$  given by

$$A := \begin{pmatrix} \mathbb{D}\text{iv} \\ \overline{\mathbb{C}\text{url }} \\ \mathbb{B}_n \end{pmatrix} \in \mathbb{R}^{\dim H_S+1, \dim H_S}, \quad (18)$$

where the  $\overline{\mathbb{C}\text{url }}$  operator is naturally extended to the whole space  $H_S$ . The operator  $A$  has full rank  $\dim H_S$ . Moreover, we see by (6) that  $(\rho, \omega, v)^T$  is in the image of  $A$  if and only if  $\rho$  and  $v$  fulfill the compatibility condition (17). In this case, the representation of  $u$  in terms of  $(\rho, \omega, v)^T$  is given by  $u = A^\dagger(\rho, \omega, v)^T$ , where  $A^\dagger = (A^T A)^{-1} A^T$  denotes the pseudoinverse of  $A$ .

**Proposition 2.1** *There is a one-to-one correspondence between the spaces  $H_S$  and*

$$V_S := \{(\rho, \omega, v)^T : \mathbf{1}_{\dim H_V}^T \rho = \mathbf{1}_{\dim \partial H_S}^T v\}, \quad (19)$$

where  $u \in H_S$ ,  $\rho = \mathbb{D}\text{iv } u$ ,  $\omega = \overline{\mathbb{C}\text{url }} u$ ,  $v = \mathbb{B}_n u$ , and

$$u = A^\dagger(\rho, \omega, v)^T \quad (20)$$

**Remark** In practice, we do not compute  $u = A^\dagger(\rho, \omega, v)^T$  which is ill-conditioned. Rather, we solve both the Neumann problem (14) and the Dirichlet problem (15), and insert the solutions into (7).

### 2.4 Extended Flow Decompositions

We take a closer look at the representation (20) by further decomposing the space  $V_S$  defined in (20). As a result, we

obtain a definition of *laminar flows*, insight into the influence of boundary values, and further orthogonality relations.

The orthogonal decomposition theorem (7) shows that the two potential functions  $\psi, \phi$  can be computed through a vector field  $u$  and its normal boundary flow  $u_{\partial\Omega}$ , and that the representation (13) holds. This decomposition can be rewritten in a meaningful way using the representation  $(\rho, \omega, v)^T$ :

$$(\rho, \omega, v)^T = (\rho, 0, v)^T + (0, \omega, 0)^T \quad (21)$$

Obviously, the two components,  $(\rho, 0, v)^T$  and  $(0, \omega, 0)^T$ , are in  $V_S$ . While  $(\rho, 0, v)^T$  is curl-free, component  $(0, \omega, 0)^T$  is divergence-free. Let  $c_\rho$  and  $c_\omega$  denote constants proportional to the mean of the divergence and the curl of  $u$ , that is

$$c_\rho := \mathbf{1}_{\dim H_V}^T \rho = \mathbf{1}_{\dim H_V}^T \operatorname{Div} u, \quad (22)$$

$$c_\omega := \mathbf{1}_{\dim H_P^o}^T \omega = \mathbf{1}_{\dim H_P^o}^T \operatorname{Curl} u. \quad (23)$$

Using these averaged quantities, we can further decompose the flow  $u \in H_S$ , represented by  $(\rho, \omega, v)^T \in V_S$ :

$$(\rho, \omega, v)^T = (c_\rho, c_\omega, v)^T + (\rho^o, 0, 0)^T + (0, \omega^o, 0)^T, \quad (24)$$

where  $\mathbf{1}_{\dim H_V}^T \rho^o = \mathbf{1}_{\dim H_P^o}^T \omega^o = 0$ . Accordingly, we define the components

$$u = u^c + u_d^o + u_c^o$$

where  $u^c := A^\dagger(c_\rho, c_\omega, v)^T$ ,  $u_d^o := A^\dagger(\rho^o, 0, 0)^T$  and  $u_c^o := A^\dagger(0, \omega^o, 0)^T$ . Vector  $u^c$  and  $(c_\rho, c_\omega, v)^T$ , respectively, represent the *basic pattern* of the non-rigid flow  $u$  and its boundary distribution, while  $u_d^o, u_c^o$  and  $(\rho^o, 0, 0)^T, (0, \omega^o, 0)^T$  are related to *oscillating flow patterns* that are curl-free and divergence-free, respectively. Due to non-vanishing spatial averages of  $c_\rho, c_\omega$ , the component  $u^c$  determines the global structure of the flow field, justifying the term basic flow pattern. It is easy to verify that orthogonality between the components  $u_d^o$  and  $u_c^o$  is preserved

$$\langle u_d^o, u_c^o \rangle = 0,$$

while  $u^c$  and  $u_c^o, u_d^o$  are not orthogonal.

We summarize these properties, thereby extending Theorem 2.1:

**Proposition 2.2** *For any 2D vector field  $u \in H_S$  and  $\mathbb{B}_n u \neq 0$ , the decomposition (24) of  $u$  admits the representation in terms of functions  $\psi^c, \phi^c, \psi^o, \phi^o$*

$$u = (\overline{\mathbb{G}}\psi^c + \mathbb{G}^\perp\phi^c) + \overline{\mathbb{G}}\psi^o + \mathbb{G}^\perp\phi^o, \quad \mathbb{B}_n u = \mathbb{B}_n \overline{\mathbb{G}}\psi^c \quad (25)$$

where  $\phi_{\partial\Omega}^c = \phi_{\partial\Omega}^o = 0$ ,  $\mathbb{B}_n \overline{\mathbb{G}}\psi^o = 0$ , and  $\Delta_D \psi^c \equiv \text{constant}$ ,  $\Delta_C \phi^c \equiv \text{constant}$ . This representation is unique up to two

constants of  $\psi^c$  and  $\psi^o$ , respectively. Moreover, the orthogonality relation

$$\langle \overline{\mathbb{G}}\psi^o, \mathbb{G}^\perp\phi^o \rangle = 0 \quad (26)$$

holds.

While the components of the decomposition (24) and (25) are easy to interpret, a single orthogonality relation (26) only holds. To improve the latter situation, we consider the alternative decomposition

$$(\rho, \omega, v)^T = (c_\rho, 0, v)^T + (\rho^o, 0, 0)^T + (0, \omega, 0)^T. \quad (27)$$

The corresponding components of  $u \in H_S$  are denoted as

$$u = u_d^c + u_d^o + u_c$$

where  $u_d^c := A^\dagger(c_\rho, 0, v)^T$ ,  $u_d^o := A^\dagger(\rho^o, 0, 0)^T$  and  $u_c := A^\dagger(0, \omega, 0)^T$ . As will be shown below, this decomposition provides the basis for representing any vector field, under additional conditions to be specified, by three mutually orthogonal components. We first summarize the properties of (27):

**Proposition 2.3** *For any 2D vector field  $u \in H_S$  and  $\mathbb{B}_n u \neq 0$ , the decomposition (27) of  $u$  admits the representation in terms of functions  $\psi^c, \psi^o, \phi$*

$$u = \overline{\mathbb{G}}\psi^c + \overline{\mathbb{G}}\psi^o + \mathbb{G}^\perp\phi, \quad \mathbb{B}_n u = \mathbb{B}_n \overline{\mathbb{G}}\psi^c \quad (28)$$

where  $\phi_{\partial\Omega} = 0$ ,  $\mathbb{B}_n \overline{\mathbb{G}}\psi^o = 0$ , and  $\Delta_D \psi^c \equiv \text{constant}$ . This representation is unique up to two constants of  $\psi^c$  and  $\psi^o$ , respectively. Moreover, the orthogonality relations

$$\langle \overline{\mathbb{G}}\psi^o, \mathbb{G}^\perp\phi \rangle = 0, \quad \langle \overline{\mathbb{G}}\psi^c, \mathbb{G}^\perp\phi \rangle = 0$$

hold.

It remains to work out conditions under which the flow components  $\overline{\mathbb{G}}\psi^c$  and  $\overline{\mathbb{G}}\psi^o$  are orthogonal, too. By Green's theorem (3), we have

$$\langle \overline{\mathbb{G}}\psi^o, \overline{\mathbb{G}}\psi^c \rangle = -\langle \psi^o, \Delta_D \psi^c \rangle + \langle \psi^o, v \rangle_{\partial\Omega}$$

Taking into account the compatibility condition (17),  $\mathbf{1}_{\dim H_V}^T \Delta_D \psi^c = \mathbf{1}_{\dim \partial H_S}^T v$ , we observe that the right hand side is invariant with respect to an arbitrary additive constant  $C$  of  $\psi^o$ :

$$\begin{aligned} & -\langle \psi^o + C, \Delta_D \psi^c \rangle + \langle \psi^o + C, v \rangle_{\partial\Omega} \\ &= -\langle \psi^o, \Delta_D \psi^c \rangle + \langle \psi^o, v \rangle_{\partial\Omega} \\ & \quad + C(-\mathbf{1}_{\dim H_V}^T \Delta_D \psi^c + \mathbf{1}_{\dim \partial H_S}^T v) \\ &= -\langle \psi^o, \Delta_D \psi^c \rangle + \langle \psi^o, v \rangle_{\partial\Omega}. \end{aligned}$$

Hence, fixing this constant by setting  $\langle \psi^o, v \rangle = 0$ , we obtain

$$-\langle \psi^o, \Delta_D \psi^c \rangle + \langle \psi^o, v \rangle_{\partial\Omega} = -c_\rho \mathbf{1}_{\dim H_V}^\top \psi^o,$$

because  $\Delta_D \psi^c$  is constant by Proposition 2.3. It follows that  $\langle \bar{\mathbb{G}}\psi^o, \bar{\mathbb{G}}\psi^c \rangle = 0$  if  $c_\rho = 0$ . This means that the total divergence of flow  $u$  is zero, and that the flow entering and leaving the domain  $\Omega$  is balanced

$$\mathbf{1}_{\dim H_V}^\top \operatorname{Div} u = \mathbf{1}_{\dim \partial H_S}^\top v = 0.$$

**Proposition 2.4** Suppose  $u \in H_S$  is a 2D vector field with  $\mathbb{B}_n u \neq 0$ , and that the balanced boundary flow condition

$$\mathbf{1}_{\dim \partial H_S}^\top \mathbb{B}_n u = 0$$

holds. Then  $u$  can be represented in terms of functions  $\psi^c, \psi^o, \phi$

$$u = \bar{\mathbb{G}}\psi^c + \bar{\mathbb{G}}\psi^o + \mathbb{G}^\perp \phi, \quad \mathbb{B}_n u = \mathbb{B}_n \bar{\mathbb{G}}\psi^c, \quad (29)$$

where  $\phi_{\partial\Omega} = 0$ ,  $\mathbb{B}_n \bar{\mathbb{G}}\psi^o = 0$ , and  $\Delta_D \psi^c \equiv 0$ . This representation is unique up to two constants of  $\psi^c$  and  $\psi^o$ , respectively, and all three components  $\bar{\mathbb{G}}\psi^c$ ,  $\bar{\mathbb{G}}\psi^o$  and  $\mathbb{G}^\perp \phi$ , are mutually orthogonal.

Note that the basic part  $\bar{\mathbb{G}}\psi^c$  turns out to be the *laminar flow*, i.e. it is both divergence and curl free.

As a consequence of Proposition 2.4, we can refine the decomposition (13) of the vector field space  $H_S$ . To this end, we define further subspaces in addition to (11) and (12):

- $H_{S,\bar{o}} \subset H_S$ : subspace of vector fields with  $\mathbf{1}_{\dim \partial H_S}^\top \mathbb{B}_n u = 0$ ,
- $S_{ir,o} \subset S_{ir}$ : subspace of irrotational vector fields with zero boundary flow,
- $S_{ir,C} \subset S_{ir}$ : subspace of irrotational vector fields with constant divergence,
- $S_{div,0}$ : subspace of vector fields with vanishing divergence,
- $S_{lam}$ : subspace of vector fields with vanishing divergence and curl.

Based on these definitions, we summarize consequences of Proposition 2.4:

**Corollary 2.1** 2D vector fields  $u \in H_S$  admit the following decompositions:

$$H_S = (S_{ir,C} + S_{ir,o}) \oplus S_{sol}, \quad (30)$$

$$H_{S,\bar{o}} = S_{ir,C} \oplus S_{ir,o} \oplus S_{sol}, \quad (31)$$

$$S_{div,0} = S_{lam} \oplus S_{sol}. \quad (32)$$

### 3 Variational Approaches

In this section, we present and discuss various variants of the following variational approach to optical flow estimation:

$$\min_{u \in H_S} F(u) := \|I_1(x+u) - I_2(x)\|_{H_V}^2 + L(u) \quad (33)$$

Here,  $I_1, I_2 \in H_V$  are subsequent images of a given sequence, and  $L(u)$  is a regularizing term to be specified below, which makes the variational problem well-posed.

We point out that the data term—the first term in (33)—could be made robust against outliers by using some robust estimators or the  $L^1$ -norm [4]. In this paper, however, we focus on higher-order regularization in connection with the representation (7).

#### 3.1 Data Term

In order to alleviate the local minima problem and to capture large motions, we apply the standard procedure of minimizing  $F(u)$  using a sequence of linearizations of the data term

$$F^l(u^l) := \|\bar{\mathbb{G}}I_1^l \cdot u^l + \partial_t I^l\|_{H_V}^2 + L(u^l), \quad (34)$$

where  $\{I_1^l, I_2^l\}_{l=0,1,\dots,m}$  denote linear scale-space representations of a given image pair, and  $\partial_t I^l = I_1^l(x) - I_2^l(x - u^{l+1}(x))$ .

In this connection, the prolongation operator transferring various quantities to the next finer grid deserves special attention, in order to preserve properties based on the decomposition (7). A corresponding constrained interpolation scheme will be detailed in Sect. 5.3.

#### 3.2 Div-Curl Regularization

We wish to apply the following second-order regularizer (cf. the discussion of related work in Sect. 1):

$$\begin{aligned} & \int_{\Omega} \lambda_1 |\nabla \operatorname{div} u|^2 + \lambda_2 |\nabla \operatorname{curl} u|^2 dx \\ &= \int_{\Omega} \lambda_1 |\nabla \Delta \psi|^2 + \lambda_2 |\nabla \Delta \phi|^2 dx \end{aligned} \quad (35)$$

where  $\lambda_1$  and  $\lambda_2$  are two positive constants. This term measures the variation of the basic flow components divergence and curl, but *does not penalize* the components themselves. However, both standard finite differences or finite elements discretization lead to finite-dimensional representations which do not satisfy (7) and (10). As a result, penalizing one component may affect the other component too. Therefore, we adopt the framework of Sect. 2.2 which leads

to the following discretization of (35):

$$\begin{aligned} L(u) &= L_{\text{div}}(u) + L_{\text{curl}}(u) \\ &= \lambda_1 \|\overline{\mathbb{G}} \text{Div } u\|_{H_S}^2 + \lambda_2 \|\mathbb{G} \overline{\text{Curl}} u\|_{H_E}^2 \end{aligned} \quad (36)$$

$$= \lambda_1 \|\overline{\mathbb{G}} \Delta_D \psi\|_{H_S}^2 + \lambda_2 \|\mathbb{G} \Delta_C \phi\|_{H_E}^2 \quad (37)$$

### 3.3 Potential Based Non-rigid Flow Estimation

For the general non-rigid flow estimation, we consider the functional

$$\min_{u \in H_S} F(u) := \|I_1(x + u) - I_2(x)\|_{H_V}^2 + L_{\text{div}}(u) + L_{\text{curl}}(u) \quad (38)$$

Inserting the decomposition (7) and (37), we obtain the minimization problem

$$\begin{aligned} \min_{\psi, \phi} F(\psi, \phi) &= \|I_1(x + \overline{\mathbb{G}}\psi + \mathbb{G}^\perp\phi) - I_2(x)\|_{H_V}^2 \\ &\quad + \lambda_1 \|\overline{\mathbb{G}} \Delta_D \psi\|_{H_S}^2 + \lambda_2 \|\mathbb{G} \Delta_C \phi\|_{H_E}^2 \end{aligned} \quad (39)$$

subject to the linear constraints

$$\mathbf{1}_{\dim H_{V+\partial V}}^T \psi = 0, \quad \phi_{\partial\Omega} = 0 \quad (40)$$

Note that the first constraint fixes the free constant mentioned in Theorem 2.1. Furthermore, the vector fields in (39) are elements of orthogonal subspaces (13), and thus may be determined in parallel by subspace correction methods.

### 3.4 Estimation of Solenoidal Flows

An important special case, particularly in applications of experimental fluid dynamics, concerns the estimation of divergence-free flows. In this case the decomposition (29) reduces to (cf. (32)):

$$u = \overline{\mathbb{G}}\psi^c + \mathbb{G}^\perp\phi := u_d^c + u_c \quad (41)$$

with the laminar flow  $u_d^c = \overline{\mathbb{G}}\psi^c$  which only depends on the boundary flow  $\mathbb{B}_n u$ :

$$\Delta_D \psi^c = 0, \quad \mathbb{B}_n \overline{\mathbb{G}}\psi^c = \mathbb{B}_n u. \quad (42)$$

In order to estimate solenoidal flows, we consider instead of (39) the functional

$$\min_{u \in S_{\text{div}0}} F_{\text{sol}}(u) := \|I_1(x + u) - I_2(x)\|_{H_V}^2 + L_{\text{curl}}(u). \quad (43)$$

Inserting the decomposition (41), we obtain the minimization problem:

$$\begin{aligned} \min_{\psi^c, \phi} F_{\text{sol}}(\psi^c, \phi) &= \|I_1(x + \overline{\mathbb{G}}\psi^c + \mathbb{G}^\perp\phi) - I_2(x)\|_{H_V}^2 \\ &\quad + \lambda_2 \|\mathbb{G} \Delta_C \phi\|_{H_E}^2 \end{aligned} \quad (44)$$

subject to the constraints:

$$\Delta_D \psi^c = 0, \quad \mathbf{1}_{\dim H_{V+\partial V}}^T \psi^c = 0, \quad \phi_{\partial\Omega} = 0 \quad (45)$$

Note that the vector fields of (44) are elements of orthogonal subspaces (32), and thus may be determined in parallel by subspace correction methods.

### 3.5 Third-Order Derivative Regularizers

In both variational approaches (39) and (44) third-order regularizers appear in the energy functional. A common method to reduce the order of the regularizer is to use auxiliary variables  $\xi_1 = \Delta_D \psi$  and  $\xi_2 = \Delta_C \phi$  resulting in first-order terms:

$$L_{\text{div}} = \lambda_1 \|\overline{\mathbb{G}}\xi_1\|_{H_S}^2, \quad L_{\text{curl}} = \lambda_2 \|\mathbb{G}\xi_2\|_{H_E}^2 \quad (46)$$

$$\text{s.t. } \xi_1 = \Delta_D \psi, \quad \xi_2 = \Delta_C \phi$$

In principle, this has the advantage to decrease the order of the regularizers. On the other hand, imposing the equations  $\xi_1 = \Delta_D \psi$ ,  $\xi_2 = \Delta_C \phi$  as hard constraints requires a careful analysis of the underlying continuous setting in order to avoid a mismatch of spaces and boundary constraints. Therefore, such equations are mostly applied in a least-squares sense in the literature, which introduces additional errors. In contrast, through the mimetic finite-difference method it is possible to directly obtain problem discretizations which are both accurate and stable.

## 4 Well-Posedness and Stability

In this section, we analyse well-posedness of the variational approaches discussed in Sect. 3. To this end, we state the conditions under which the respective functionals are strictly convex. This will be done for a single level  $l$  in (34), and in terms of vector fields  $u$  due to the unique representations stated in Theorem 2.1 and Proposition 2.4. These representations also allow us to point out in Sect. 4.3 a potential source of instability in connection with the higher-order regularizer from Sect. 3.2. This result appears to be new in the literature. Furthermore, our experimental results showed that removing this instability as developed below, is numerically significant.

In order to compactly state the various conditions for well-posedness, we complement the list of subspaces defined at the end of Sect. 2.4. To this end, we define the linear operator

$$G := (\overline{\mathbb{G}} I_1 \cdot),$$

and use the notation  $N(A)$  for the null-space of a linear operator  $A$ :

- $S_{\text{sol},C} \subset S_{\text{sol}}$ : subspace of solenoidal vector fields with constant curl,
  - $H_{S,C} \subset H_S$ : subspace of vector fields
- $$H_{S,C} := S_{\text{ir},C} + S_{\text{sol},C} = N(\overline{\mathbb{G}} \text{Div}) \cap N(\overline{\mathbb{G}} \text{Curl}),$$
- $S_{G0} \subset H_S$ : subspace of vector fields
- $$S_{G0} = \{u \mid Gu = 0\}.$$

#### 4.1 Well-Posedness of General Flows

The variational approach (33) for estimating general flows amounts to the unconstrained convex minimization problem:

$$\begin{aligned} \min_{u \in H_S} F(u) &= \|Gu + \partial_t I\|_{H_V}^2 + \lambda_1 \|\overline{\mathbb{G}} \text{Div} u\|_{H_S}^2 \\ &\quad + \lambda_2 \|\overline{\mathbb{G}} \text{Curl} u\|_{H_E}^2 \end{aligned} \quad (47)$$

As a consequence, the following is immediate:

**Proposition 4.1** Problem (33) is well-posed if and only if

$$S_{G0} \cap H_{S,C} = \{0\}$$

As the subspace  $H_{S,C}$  is fixed with the problem dimension, this condition requires a sufficiently high spatial variation of the grayvalue image  $I$  to obtain well-posedness. A counter-example is given by any image  $I$  with  $\Delta_D I = \text{Curl} \overline{\mathbb{G}}^\perp I = C$ , because for the vector field  $\overline{\mathbb{G}}^\perp I \in H_E$  the inner product with  $\overline{\mathbb{G}} I \cdot \overline{\mathbb{G}}^\perp I$ , computed by summing up the corresponding local expressions over all cells (see Fig. 1), vanishes.

#### 4.2 Well-Posedness on Solenoidal Flows

The variational approach (43) for estimating divergence-free flows amounts to a convex quadratic minimization problem with linear equality constraints. Expressing the restriction  $u \in S_{\text{lam}} \oplus S_{\text{sol}}$  through the constraint  $\text{Div} u = 0$ , we reformulate (43):

$$\min_{u \in H_S} F_{\text{sol}}(u) = \|Gu + \partial_t I\|_{H_V}^2 + \lambda \|\overline{\mathbb{G}} \text{Curl} u\|_{H_E}^2 \quad (48)$$

$$\text{s.t. } \text{Div} u = 0$$

As a consequence, the condition for well-posedness reads:

**Proposition 4.2** Problems (43) and (48) are well-posed if and only if

$$S_{G0} \cap (S_{\text{lam}} \oplus S_{\text{sol},C}) = \{0\}$$

Note that Problem (48) apparently gives rise to three relevant null-spaces,  $S_g$ ,  $S_{\text{sol},C}$ , and  $S_{\text{lam}} \oplus S_{\text{sol}}$ . However, because  $S_{\text{sol},C} \subset S_{\text{sol}}$ , we have

$$S_{\text{sol},C} \cap (S_{\text{lam}} \oplus S_{\text{sol}}) = S_{\text{lam}} \oplus S_{\text{sol},C}.$$

#### 4.3 Stability

It is well-known that existence of a unique solution, as established in the previous section, does not say much about numerical stability. Indeed, inspection of the second-order regularizer (35) reveals a particular sensitivity of  $u$  with respect to the image data and suggests using a corresponding regularizer.

To motivate this additional term, we rewrite the estimation functional using the representation  $(\rho, \omega, u_{\partial\Omega})^T$  (cf. Proposition 2.1):

$$\begin{aligned} \min_{\rho, \omega, u_{\partial\Omega}} F(u) &= \|GA^\dagger(\rho, \omega, u_{\partial\Omega})^T \partial_t I\|^2 \\ &\quad + \lambda_1 \|\nabla \rho\|^2 + \lambda_2 \|\nabla \omega\|^2. \end{aligned} \quad (49)$$

We consider the extended decomposition due to Theorem 2.3 and (30). Considering (27), the variance of divergence and curl field related to the two components  $(\rho^o, 0, 0)^T$  and  $(0, \omega, 0)^T$  can be penalized and constrained by the respective regularizers. However, for the last part  $(c_\rho, 0, v)^T$  which is curl-free and has constant divergence, both regularization terms are not effective.

The discussion in Sect. 2.4 showed that this part only depends on the normal flow at the boundary  $u_{\partial\Omega}$ . In fact,  $(c_\rho, 0, v)^T$  is only weakly constrained by the data term, that is the gradient field of image data  $I$  at the boundary whose estimate is noisy and unreliable. Therefore, in practice, it turned out to be useful to reduce this sensitivity of  $u$  by including a regularizer which additionally constrains the boundary values:

$$\int_{\partial\Omega} (\partial_n u)^2 dl. \quad (50)$$

This constraint term favors continuity of vector field  $u(\Omega)$  between the boundary and the interior domain. By virtue of the orthogonal decomposition, it can be directly expressed in terms of  $\psi$

$$\int_{\partial\Omega} |\partial_n(\nabla \psi)|^2 dl. \quad (51)$$

The discrete version of this regularizer reads

$$\|\mathbb{P} \overline{\mathbb{G}} \psi\|_{bc}^2 \quad (52)$$

where the respective matrix  $\mathbb{P}$  represents the operator  $\partial_n$  in (51), and  $\|\cdot\|_{bc}$  is the norm evaluating elements along the boundary  $\partial\Omega$ .

## 5 Algorithms and Implementation

In this paper, we apply the space decomposition method to restore the two potential fields  $\phi(\Omega)$  and  $\psi(\Omega)$  directly. This

method provides a general framework for analysing domain decomposition and multigrid methods [26, 27]. The essence is to decompose the solution space into a sum of subspaces and then solve the original optimization problem sequentially or in parallel in each subspace. Extensions to some convex optimization problems were presented in [23], and convergence rates are analyzed in [21, 22, 24].

We describe the space decomposition method and its application to our approach in Sects. 5.1 and 5.2. Subsequently, we detail in Sects. 5.3 and 5.4 a multi-level representation of flow fields adapted to the orthogonal decomposition.

### 5.1 Iterative Subspace Corrections

Suppose that for a general convex optimization problem

$$\min_{u \in V} F(u), \quad (53)$$

the solution function space  $V$  can be decomposed into a sum of subspaces

$$V = V_1 + V_2 + \cdots + V_m. \quad (54)$$

For any  $u \in V$ , there exist  $u_i \in V_i$ , such that  $u = \sum_{i=1}^m u_i$ . Conversely, if  $u_i \in V_i$ , then  $\sum_{i=1}^m u_i \in V$ . Note that in general the sum is not the direct sum, and the decomposition of  $u$  is not unique.

There are two versions of iterative algorithms, the Parallel Subspace Corrections (PSC) and the Successive Subspace Corrections (SSC). In each step, PSC and SSC compute the next iterate in  $V$  through searching each subspaces  $V_i$ ,  $i = 1, \dots, m$ , in parallel or sequentially, respectively. With suitable assumptions about the objective function  $F(u)$  and the space decomposition scheme, both algorithms converge. As we do not focus on parallel implementations in this work, we adopted SSC which, in this case, converges faster.

#### Algorithm 5.1 (Successive Subspace Corrections)

- Step 1. Choose  $u_i^0 \in V_i$ .
- Step 2. For the  $n$ -th iteration, compute  $\hat{u}_i^{n+1} \in V_i$  sequentially for  $i = 1, \dots, m$ , by minimization:

$$\begin{aligned} F\left(\sum_{1 \leq k < i} u_k^{n+1} + \hat{u}_i^{n+1} + \sum_{i < k \leq m} u_k^n\right) \\ \leq F\left(\sum_{1 \leq k < i} u_k^{n+1} + v_i + \sum_{i < k \leq m} u_k^n\right), \quad \forall v_i \in V_i. \end{aligned} \quad (55)$$

Choose  $u_i^{n+1} \in V_i$ ,  $i = 1, \dots, m$ , such that

$$\|u_i^{n+1} - \hat{u}_i^{n+1}\|_V \leq \epsilon_0 \|u_i^n - \hat{u}_i^{n+1}\|_V, \quad 0 \leq \epsilon_0 \leq 1. \quad (56)$$

- Step 3. Go to the next iteration.

In practice, we choose  $u_i^{n+1} = (1 - \epsilon_0)\hat{u}_i^{n+1} + \epsilon_0 u_i^n$ , with  $\epsilon_0 \in [0.5, 0.75]$ .

### 5.2 Application to Flow Estimation

Based on Algorithm 5.1, the estimation of general flows amounts to solving the two subproblems including the boundary stability term (52) with a penalty parameter  $\lambda_3$ ,

$$\begin{aligned} \min_{\psi} \widetilde{F}(\psi, \bar{\phi}) = & \|I(x + \overline{\mathbb{G}}\psi + \mathbb{G}^\perp \bar{\phi}) - I(x)\|_{H_V}^2 \\ & + \lambda_1 \|\overline{\mathbb{G}}\Delta_D \psi\|_{H_S}^2 + \lambda_3 \|\mathbb{P}\overline{\mathbb{G}}\psi\|_{bc}^2, \end{aligned} \quad (57)$$

$$\begin{aligned} \min_{\phi} \widetilde{F}(\bar{\psi}, \phi) = & \|I(x + \overline{\mathbb{G}}\bar{\psi} + \mathbb{G}^\perp \phi) - I(x)\|_{H_V}^2 \\ & + \lambda_2 \|\mathbb{G}\Delta_C \phi\|_{H_E}^2, \end{aligned} \quad (58)$$

and subject to the linear constraint (40) for  $\psi$ , whereas the constraint for  $\phi$  is directly encoded by the discretization. Here  $\bar{\psi}$  and  $\bar{\phi}$  in (57) and (58) are fixed variables at each iteration. Each subproblem is an convex quadratic problem to which the preconditioned conjugate gradient iteration [19] was applied. The  $\psi$ -step includes a simple projection due to the linear constraint in (40).

Concerning estimation of divergence-free flows, approach (44) together with (45) requires as part of Algorithm 5.1 to solve a linearly constrained quadratic problem in the subspace of laminar flows. To this end, the Augmented Lagrangian Method is applied. For details, we refer to [3]. The corresponding augmented Lagrangian function for the  $\psi$ -subproblem reads:

$$\begin{aligned} L_{\bar{\phi}}(\psi^c, r) = & \|I(x + \overline{\mathbb{G}}\psi^c + \mathbb{G}^\perp \bar{\phi}) - I(x)\|^2 \\ & + \langle r, \Delta_D \psi^c \rangle + \frac{c}{2} \|\Delta_D \psi^c\|_{H_V}^2 + \lambda_3 \|\mathbb{P}\overline{\mathbb{G}}\psi^c\|_{bc}^2 \end{aligned} \quad (59)$$

with  $\bar{\phi}$  being fixed at each iteration step. Direct incorporation into the augmented Lagrangian iteration of the remaining linear equality  $\sum_{H_V + \partial V} \psi = 0$  in (45) would destroy the sparsity of the matrix of the penalty term and, in turn, the efficiency of the sparse solver. Instead, we simply remove the average from iterates  $(\psi^c)^n$  as a simple post-processing step.

In practice, the augmented Lagrangian iteration converged in less than 10 iterations.

### 5.3 Multi-level Implementation

Related to Sect. 3.1, we detail in this and in the following section the multi-level handling of flow fields in terms of potential functions  $\psi, \phi$ .

According to Sect. 2.2, discrete fields of divergence  $(\operatorname{Div} u)^l$ ,  $l = 1, \dots, m$ , are elements of the space  $H_V$ , and fields  $(\overline{\operatorname{Curl}} u)^l$ ,  $l = 1, \dots, m$ , are in  $H_P^o$ .

As described in [16, 18], two image pyramids  $\{I_i^l\}_{l=1,\dots,m}$ ,  $i = 1, 2$ , are constructed.  $l = 0$  denotes the original image, and  $l = m$  denotes the coarsest level. At level  $l$ , given potential fields  $\tilde{\psi}^l$ ,  $\tilde{\phi}^l$  and the velocity field  $\tilde{u}^l = \overline{\mathbb{G}}\psi^l + \mathbb{G}^\perp\tilde{\phi}^l$ , image  $I_2^l$  is warped to  $\tilde{I}_2^l = I_2^l(x - \tilde{u}^l)$ . The image flow between the two images  $\tilde{I}_1^l$  and  $I_2^l$  is assumed to be small enough to allow for accurate linearization:

$$\partial_t I^l = I_1^l - \tilde{I}_2^l, \quad (60)$$

$$\Delta_u^l = \overline{\mathbb{G}}I_1^l \cdot (u^l - \tilde{u}^l), \quad (61)$$

$$\Delta_{\psi,\phi}^l = \overline{\mathbb{G}}I_1^l \cdot (\overline{\mathbb{G}}(\psi^l - \tilde{\psi}^l) + \mathbb{G}^\perp(\phi^l - \tilde{\phi}^l)). \quad (62)$$

The residual motion field  $u^l$ , in terms of  $\overline{\mathbb{G}}\psi^l + \mathbb{G}^\perp\phi^l$ , is estimated by solving the problem

$$\begin{aligned} \min_{\psi^l, \phi^l} F(\psi^l, \phi^l) = & \|\Delta_{\psi,\phi}^l + \partial_t I^l\|_{H_V}^2 + \lambda_1 \|\overline{\mathbb{G}}\Delta_D \psi^l\|_{H_S}^2 \\ & + \lambda_2 \|\mathbb{G}\Delta_C \phi^l\|_{H_E}^2 + \lambda_3 \|\overline{\mathbb{G}}\psi^l\|_{bc}^2 \end{aligned} \quad (63)$$

The minimizer  $\psi^l$ ,  $\phi^l$  and  $u^l$  are postprocessed to yield the initialization  $\tilde{\psi}^{l-1}$ ,  $\tilde{\phi}^{l-1}$  and  $\tilde{u}^{l-1}$  of the next finer level  $l - 1$ , as discussed in the following section. The whole process is started at the coarsest level  $m$  with  $\tilde{\psi}^m = 0$ ,  $\tilde{\phi}^m = 0$  and  $\tilde{u}^m = 0$ .

#### 5.4 Constrained Prolongation

It is important to preserve the subspace properties during grid transfer. Corresponding divergence- and curl-preserving interpolation schemes for vector fields are suggested in [5, 25]. In this work, however, we transfer potential fields  $\psi^l$  and  $\phi^l$  to the next level  $l - 1$ , rather than  $u^l$ .

This is done by bilinearly interpolating the divergence  $\rho^l$ , the curl  $\omega^l$ , and the boundary values of  $\psi^l$ , to obtain  $\tilde{\rho}^{l-1}$ ,  $\tilde{\omega}^{l-1}$  and  $\tilde{\psi}_{\partial\Omega}^{l-1}$  (cf. the notation of the previous section). Then  $\tilde{\psi}^{l-1}$  is computed as solution to

$$\Delta_D \psi = \tilde{\rho}^{l-1}, \quad \text{s.t. } \psi_{\partial\Omega} = \tilde{\psi}_{\partial\Omega}^{l-1}. \quad (64)$$

Analogously, we compute  $\tilde{\phi}^{l-1}$  as solution to

$$\Delta_C \phi = \tilde{\omega}^{l-1}, \quad \text{s.t. } \phi_{\partial\Omega} = 0. \quad (65)$$

The corresponding velocity field  $\tilde{u}^{l-1}$  at the next finer level  $l - 1$  is

$$\tilde{u}^{l-1} = \overline{\mathbb{G}}\tilde{\psi}^{l-1} + \mathbb{G}^\perp\tilde{\phi}^{l-1}. \quad (66)$$

## 6 Experiments

In this section, we validate our approach with few numerical experiments. A more thorough evaluation from the viewpoint of experimental fluid dynamics is beyond the scope of this work and will be reported elsewhere.

### 6.1 Error Measures

In practice, evaluating non-rigid flows by computing the average angular and norm error, respectively, induced by the inner product of the space  $(L^2(\Omega))^2 = L^2(\Omega) \times L^2(\Omega)$  [2], appeared to us too insensitive to the important flow structures. Therefore, we suggest error measures that also take into account divergence and curl of flow structures:

$$e_{\text{norm}} := \frac{\langle w, w \rangle_{\text{DC}}}{N}, \quad (67)$$

$$e_{\text{ang}} := \arccos \frac{\langle u, v \rangle_{\text{DC}} + 1}{\sqrt{\langle u, u \rangle_{\text{DC}} + 1} \sqrt{\langle v, v \rangle_{\text{DC}} + 1}}, \quad (68)$$

where we adopt the average angular and norm error measures but use the inner products of the space  $H(\text{div}; \Omega) \cap H(\text{curl}; \Omega)$  (see, e.g., [10]):

$$\begin{aligned} \langle u, v \rangle_{\text{DC}} := & \langle u, v \rangle_{H_S} + \langle \mathbb{D}\text{iv} u, \mathbb{D}\text{iv} v \rangle_{H_V} \\ & + \langle \overline{\mathbb{C}\text{url}} u, \overline{\mathbb{C}\text{url}} v \rangle_{H_P}. \end{aligned} \quad (69)$$

### 6.2 Experiment Results

In this section, we present and discuss a range of numerical experiments. Some of the vector fields depicted in corresponding figures are scaled by a factor 2 for better visibility.

#### 6.2.1 Numerical Stability

The boundary term (51) is essential for numerical stability. To demonstrate this, we warped a computer-generated gray-value function with the ground-truth flow field whose color-coded image is shown in the left panel of Fig. 2, and examined the numerical stability for the resulting variational flow estimation problem.

Omitting the boundary term by setting for the corresponding weight parameter  $\lambda_3 = 0$  leads to a numerically unstable problem. The value  $\lambda_3 = 1\text{e-}6$  results in an ill-conditioned problem and very slow convergence of the numerical iteration. Moreover, the resulting vector field shown

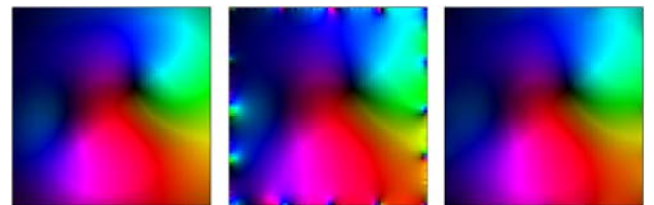


**Fig. 2** (Colour figure online) Influence of the boundary regularizer (51). *Left*: A ground-truth non-rigid velocity field shown color-coded for better visibility. *Middle*: The velocity field estimated with  $\lambda_3 = 1\text{e-}6$  for the boundary regularizer results in an ill-conditioned problem. The estimated motion field may oscillate near the boundary. *Right*: The velocity field estimated with  $\lambda_3 = 0.1$

in the middle of Fig. 2 oscillates at the boundary. The value  $\lambda_3 = 0.1$  yields a well-conditioned problem that converged after 7 iterations and results in an accurate result (Fig. 2, right panel).

### 6.2.2 Ground Truth Experiment

Figure 3 shows a particle image sequence provided by our project partners [6] through direct numerical simulation (DNS) [17] of an incompressible turbulent flow field.

The traditional Horn-Schunck method was used for comparison. We tuned the related penalty parameters by hand for the Horn-Schunck approach,  $\lambda = 0.1$ , and for our approach (44),  $\lambda_2 = 0.05$   $\lambda_3 = 0.05$  ( $\lambda_3$  weights the boundary term (52)).

Figure 3 shows the experimental results. The corresponding errors for the approach (44),  $e_{\text{norm}} = 1.49e-2$ ,  $e_{\text{ang}} = 6.94^\circ$ , are smaller than for the approach of Horn and Schunck:  $e_{\text{norm}} = 3.70e-1$ ,  $e_{\text{ang}} = 31.19^\circ$ . Note that as detailed in Sect. 6.1, these error measures include flow *derivatives* as opposed to common measures used in the literature. It can be clearly observed in Fig. 3 that our approach recovers the curl field more accurately. Furthermore, even if the image sequence data correspond to incompressible flows, ignoring the corresponding constraint leads to significant flow estimation errors of the Horn and Schunck method (mid-bottom panel).

### 6.2.3 Estimating Real Solenoidal Flows

Figure 4 shows a real world 2D turbulent flow which has been obtained in laboratory. This experimental flow has been

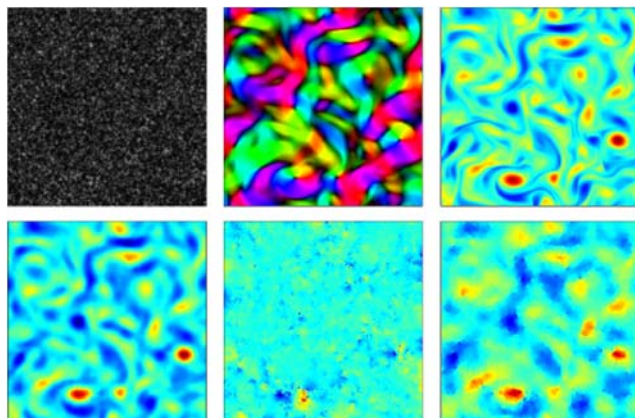


**Fig. 3** *Top left:* The first image of a particle image pair. *Top middle and right:* The ground-truth DNS-simulated divergence-free flow and its curl field. *Bottom left:* The curl field of the estimated flow, which is totally divergence-free, computed by our approach. *Bottom middle:* The divergence field, which is also the divergence-error, of the flow resulting from the Horn-Schunck method. *Bottom right:* The curl field of the flow estimated using the Horn-Schunck approach. It is apparent that the recovered curl patterns by our approach are much more accurate. The flow error measures reported in the text confirm this quantitatively

generated between two thin glass plates [15]. It is visualized through a passive scalar (a mixture of fluorescein and water) that is transported by the flow. A diffusion of the passive scalar can also be observed along time. The measurement of a slight non-vanishing divergence for this 2D flow corresponds to this diffusion effect. Rather than taking into account this effect through developing a specific data term, we focus in this paper on imposing vanishing divergence as a constraint, along with higher order regularization and adequate discretization.

Figure 4 shows the result of estimating the solenoidal flow for the real image sequence based on the multi-level framework (Sects. 5.3 and 5.4). The comparison with first-order regularization (Horn-Schunck approach) in Fig. 5 clearly reveals the superiority of our approach regarding the reconstruction of vortex structures. Furthermore, the physi-

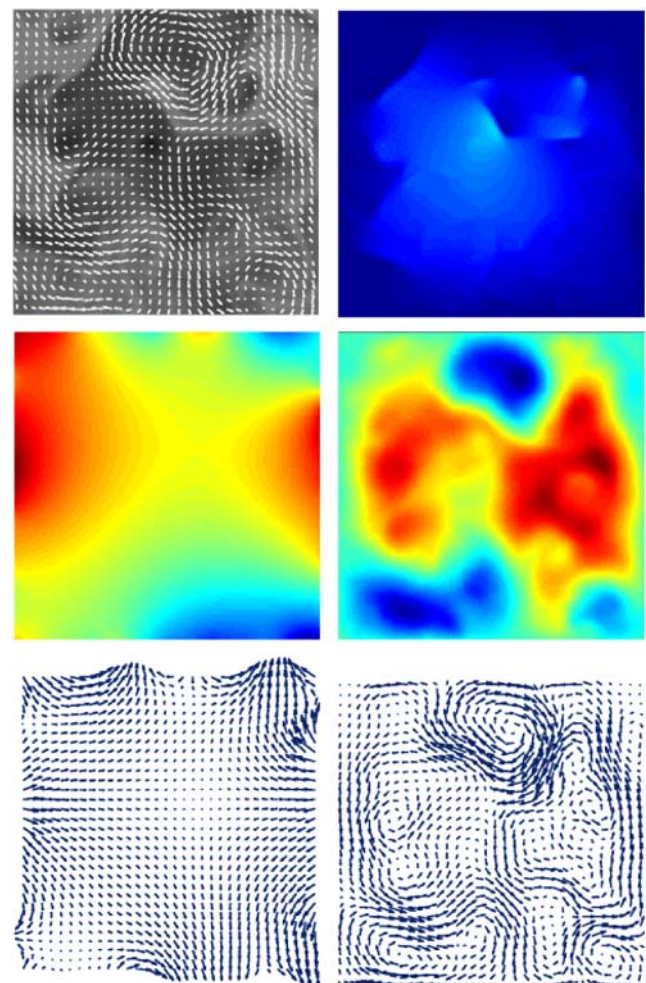


**Fig. 4** *Top left:* The first frame  $I_1$  of a real sequence together with the estimated solenoidal flow. *Top right:* The divergence field of the flow is less than  $3 \times 10^{-12}$ . *Middle left:* The potential field  $\psi_l(\Omega)$  related to the laminar flow. *Middle right:* The potential field  $\phi(\Omega)$ . *Bottom left:* The first component of flow: the laminar flow  $u_{\text{lam}}$ . *Bottom right:* The second component of flow related to potential  $\phi(\Omega)$ . A close-up view for comparison with standard regularization is depicted in Fig. 5

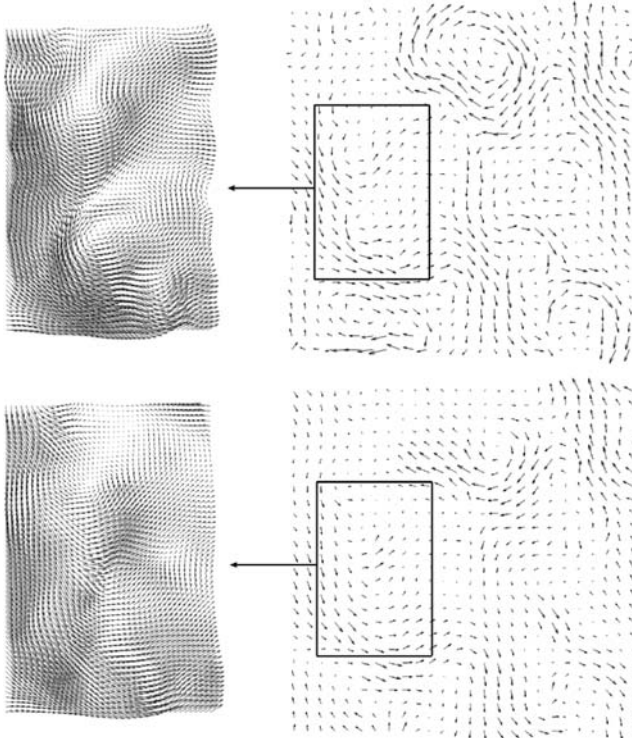


**Fig. 5** *Top:* The restored solenoidal flow  $u(\Omega)$ . *Bottom:* The restored flow  $u_{hs}(\Omega)$  using the Horn-Schunck regularization. This results clearly show that vortex structures are better recovered by our approach. Furthermore, the magnitude of the divergence is below  $10^{-11}$  throughout the image plane

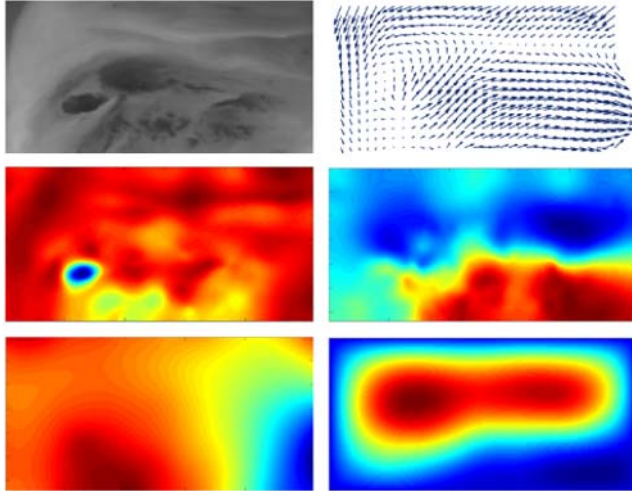


**Fig. 6** (Colour figure online) *Top:* Image  $I$  with the restored flow field  $u$ . *Middle left:* The divergence field of  $u$ . *Middle right:* The curl field of  $u$ . *Bottom left:* The potential field  $\psi(\Omega)$ . *Bottom right:* The potential field  $\phi(\Omega)$ . The divergence field reveals a “source” (blue blob) corresponding to a convective cloud cell at high altitude (see text)

cally plausible constraint of vanishing divergence is satisfied accurately.

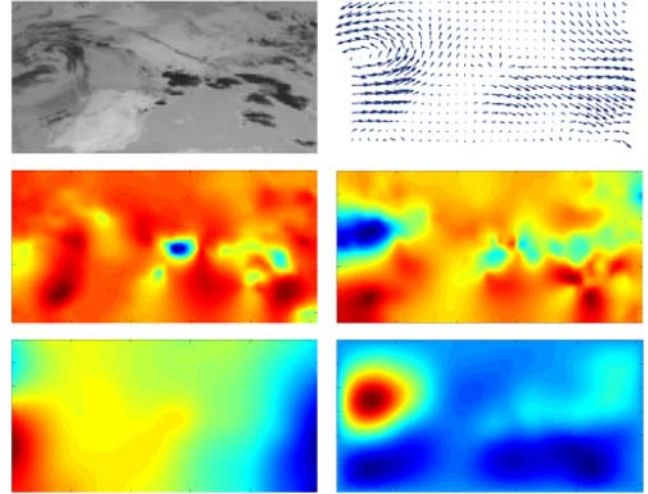


**Fig. 7** *Top:* Image  $I$  with the restored flow field  $u$ . *Middle left:* The divergence field of  $u$ . *Middle right:* The curl field of  $u$ . *Bottom left:* The potential field  $\psi(\Omega)$ . *Bottom right:* The potential field  $\phi(\Omega)$ . As in the previous figure, the potential functions provide a useful representation of qualitative properties of the flow

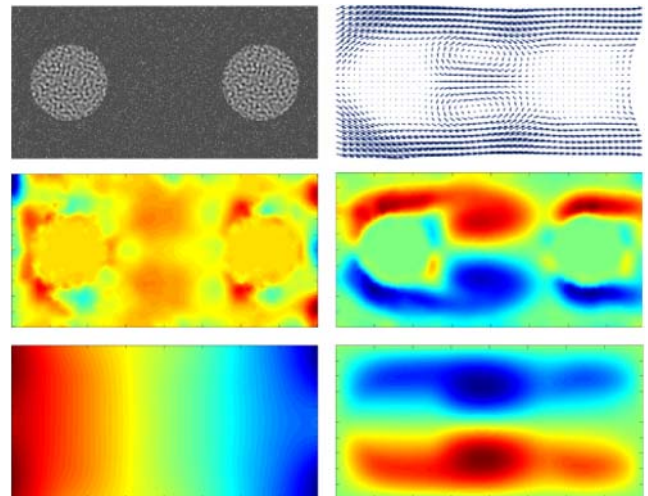


**Fig. 8** *Top:* Image  $I$  with the restored flow field  $u$ . *Middle left:* The divergence field of  $u$ . *Middle right:* The curl field of  $u$ . *Bottom left:* The potential field  $\psi(\Omega)$ . *Bottom right:* The potential field  $\phi(\Omega)$ . The two potential fields  $\psi$  and  $\phi$  are not zero at the area of two cylinders even if the flow they represent disappears in these domains. The divergence and curl fields provide clear flow information around the two cylinders

#### 6.2.4 Estimating General Non-rigid Real Flows

Figures 6 and 7 show general non-rigid flows estimated for two different real image sequences. The images show convective cloud cells at high altitudes. These clouds undergo strong upward motions until they reach the top of the atmosphere, the tropopause, and then start to decline slowly. These cells are responsible for violent showers and generate locally very strong winds. Their apparent motions correspond to highly divergent motions whose supports roughly

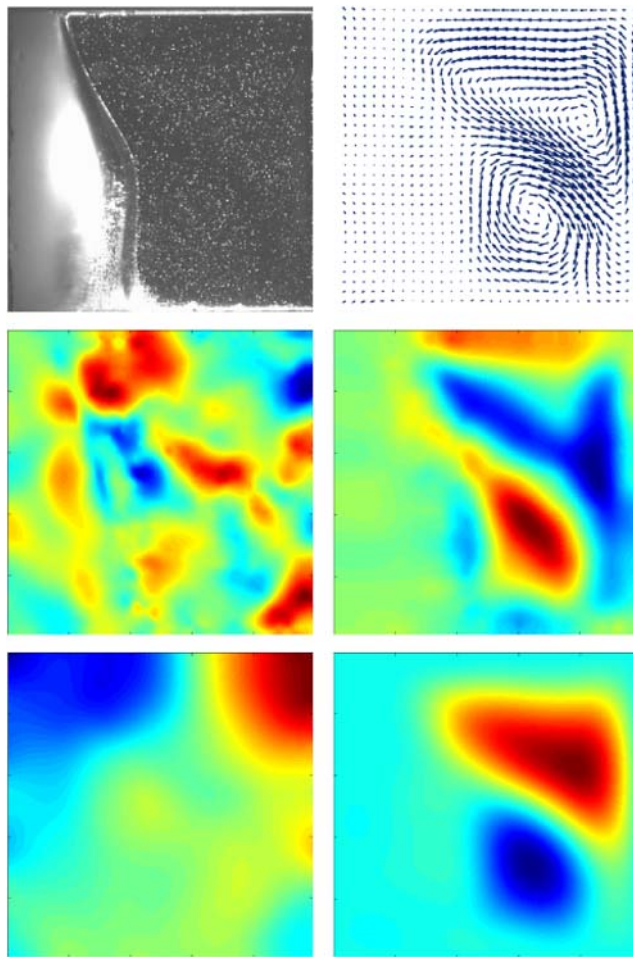


**Fig. 9** Top: Image  $I$  with the restored flow field  $u$ . Middle left: The divergence field of  $u$ . Middle right: The curl field of  $u$ . Bottom left: The potential field  $\psi(\Omega)$ . Bottom right: The potential field  $\phi(\Omega)$ . The potential functions provide a useful representation of qualitative properties of the flow

correlate with cloud boundaries. Nevertheless, such a divergent motion does not necessarily have exactly the same shape as the cloud cell. The recovered motion fields show that we have been able to estimate blobs of diverging motions which correspond to the apparent motion of these type of cloud systems.

#### 6.2.5 Application to Particle Image Velocimetry (PIV)

Figure 8 shows the result of our approach applied to a PIV image sequence from a flow around two cylinders. The divergence field and curl field inside the area of two cylinders are close to zero since the apparent motion vanishes there. Note that the two potential fields  $\psi(\Omega)$  and  $\phi(\Omega)$  are not zero in these domains, but rather the sum of  $\nabla\psi$  and  $\nabla^\perp\phi$  is.

Finally, Fig. 9 shows the results computed from a PIV image pairs of a liquid freezing experiment, recorded by Tomasz A. Kowalewski (<http://www.ippt.gov.pl/~tkowale/>).

Again, both the divergence and the curl field reveal the basic patterns of the underlying non-rigid motion.

## 7 Conclusion and Future Work

We introduced mathematically sound discrete representations of vector fields for estimating highly non-rigid flows from image sequences. The estimation is directly done in terms of component functions that decompose flows into orthogonal subspaces and reveal quantitative information of physical relevance.

Our further work will focus on the use of multigrid iterations for accelerating the subproblem solvers, on evaluations and applications from the viewpoint of experimental fluid dynamics (cf., e.g. [7, 18]), and on the extension to 3D image sequences.

**Acknowledgement** This work was supported by the European project FLUID: *Fluid Image Analysis and Description* (<http://fluid.irisa.fr/>). The authors thank Paul Ruhnau and Florian Becker (CVGPR group) for fruitful discussions and their support.

## References

1. Amodei, L., Benbourhim, M.N.: A vector spline approximation. *J. Approx. Theory* **67**(1), 51–79 (1991)
2. Barron, J.L., Fleet, D.J., Beauchemin, S.S.: Performance of optical flow techniques. *Int. J. Comput. Vis.* **12**(1), 43–77 (1994)
3. Bertsekas, D.P.: Nonlinear Programming. Athena Scientific, Belmont (1995). 2nd edn. (1999)
4. Black, M.J., Anandan, P.: The robust estimation of multiple motions: parametric and piecewise-smooth flow fields. *Comput. Vis. Image Underst.* **63**(1), 75–104 (1996)
5. Bochev, P., Shashkov, M.: Constrained interpolation (remap) of divergence-free fields. *Comput. Meth. Appl. Mech. Eng.* **194**, 511–530 (2005)
6. Carlier, I.J., Wieneke, B.: Report 1 on production and diffusion of fluid mechanics images and data. Fluid Project Deliverable, <http://fluid.irisa.fr/> (February, 2005)
7. Corpetti, T., Heitz, D., Arroyo, G., Mémin, É., Santa-Cruz, A.: Fluid experimental flow estimation based on an optical-flow scheme. *Exp. Fluids* **40**, 80–97 (2006)
8. Corpetti, T., Mémin, É., Pérez, P.: Dense estimation of fluid flows. *IEEE Trans. Pattern Anal. Mach. Intell.* **24**(3), 365–380 (2002)
9. Corpetti, T., Mémin, É., Pérez, P.: Extraction of singular points from dense motion fields: an analytic approach. *J. Math. Imag. Vision* **19**(3), 175–198 (2003)
10. Girault, V., Raviart, P.-A.: Finite Element Methods for Navier-Stokes Equations. Springer, Berlin (1986)
11. Gupta, S., Prince, J.: Stochastic models for div-curl optical flow methods. *Signal Proc. Lett.* **3**(2), 32–34 (1996)
12. Hyman, J.M., Shashkov, M.J.: Adjoint operators for the natural discretizations of the divergence, gradient and curl on logically rectangular grids. *Appl. Numer. Math.* **25**(4), 413–442 (1997)
13. Hyman, J.M., Shashkov, M.J.: Natural discretizations for the divergence, gradient, and curl on logically rectangular grids. *Comput. Math. Appl.* **33**(4), 81–104 (1997)
14. Hyman, J.M., Shashkov, M.J.: The orthogonal decomposition theorems for mimetic finite difference methods. *SIAM J. Numer. Anal.* **36**(3), 788–818 (1999). Electronic

15. Jullien, M.-C., Castiglione, P., Tabeling, P.: Intermittency of a passive tracer in the inverse energy cascade. *Phys. Rev. E* **64**(3), 035301 (2001)
16. Kohlberger, T., Mémin, E., Schnörr, C.: Variational dense motion estimation using the Helmholtz decomposition. In: Griffin, L.D., Lillholm, M. (eds.) *Scale Space Methods in Computer Vision. LNCS*, vol. 2695, pp. 432–448. Springer, Berlin (2003)
17. Pope, S.B.: *Turbulent Flows*. Cambridge University Press, Cambridge (2000)
18. Ruhnau, P., Kohlberger, T., Nobach, H., Schnörr, C.: Variational optical flow estimation for particle image velocimetry. *Exp. Fluids* **38**, 21–32 (2005)
19. Saad, Y.: *Iterative Methods for Sparse Linear Systems*, 2nd edn. Society for Industrial and Applied Mathematics, Philadelphia (2003)
20. Suter, D.: Motion estimation and vector splines. In: Proceedings of the Conference on Computer Vision and Pattern Recognition, pp. 939–942. IEEE Computer Society Press, Los Alamitos (June 1994)
21. Tai, X.-C., Espedal, M.: Rate of convergence of some space decomposition methods for linear and nonlinear problems. *SIAM J. Numer. Anal.* **35**(4), 1558–1570 (1998). Electronic
22. Tai, X.-C., Tseng, P.: Convergence rate analysis of an asynchronous space decomposition method for convex minimization. *Math. Comp.* **71**(239), 1105–1135 (2002). Electronic
23. Tai, X.-C., Xu, J.-C.: Subspace correction methods for convex optimization problems. In: Eleventh International Conference on Domain Decomposition Methods, London, 1998, pp. 130–139 (electronic). DDM.org, Augsburg, 1999.
24. Tai, X.-C., Xu, J.-C.: Global and uniform convergence of subspace correction methods for some convex optimization problems. *Math. Comp.* **71**(237), 105–124 (2002). Electronic
25. Tóth, G., Roe, P.L.: Divergence- and curl-preserving prolongation and restriction formulas. *J. Comput. Phys.* **180**(2), 736–750 (2002)
26. Xu, J.: Iterative methods by space decomposition and subspace correction: a unifying approach. *SIAM Rev.* **34**, 581–613 (1992)
27. Xu, J.-C.: *Theory of Multilevel Methods*. PhD thesis, Cornell University (May 1989)
28. Yuan, J., Ruhnau, P., Mémin, E., Schnörr, C.: Discrete orthogonal decomposition and variational fluid flow estimation. In: *Scale-Space 2005*, vol. 3459, pp. 267–278. Springer, Berlin (2005)